# Electroosmotic Flow in Nanofluidic Channels

Daniel G. Haywood, Zachary D. Harms, and Stephen C. Jacobson*

Department of Chemistry, Indiana University, 800 E. Kirkwood Ave., Bloomington, Indiana 47405-7102, United States

ABSTRACT: We report the measurement of electroosmotic mobilities in nanofluidic channels with rectangular cross sections and compare our results with theory. Nanofluidic channels were milled directly into borosilicate glass between two closely spaced microchannels with a focused ion beam instrument, and the nanochannels had half-depths (h) of 27, 54, and 108 nm and the same half-width of 265 nm. We measured electroosmotic mobilities in NaCl solutions from 0.1 to 500 mM that have Debye lengths (κ^{-1}) from 30 to 0.4 nm, respectively. The experimental electroosmotic mobilities compare quantitatively to mobilities calculated from a nonlinear solution of the Poisson−Boltzmann equation for channels with a parallel-plate geometry. For the calculations, ζ-potentials measured in a microchannel with a half-depth of 2.5 μm are used and range from −6 to −73 mV for 500 to 0.1 mM NaCl, respectively. For $\kappa h > 50$, the Smoluchowski equation accurately predicts electroosmotic mobilities in the nanochannels. However, for $\kappa h < 10$, the electrical double layer extends into the nanochannels, and due to confinement within the channels, the average electroosmotic mobilities decrease. At $\kappa h \approx 4$, the electroosmotic mobilities in the 27, 54, and 108 nm channels exhibit maxima, and at 0.1 mM NaCl, the electroosmotic mobility in the 27 nm channel ($\kappa h = 1$) is 5-fold lower than the electroosmotic mobility in the 2.5 μm channel ($\kappa h = 100$).
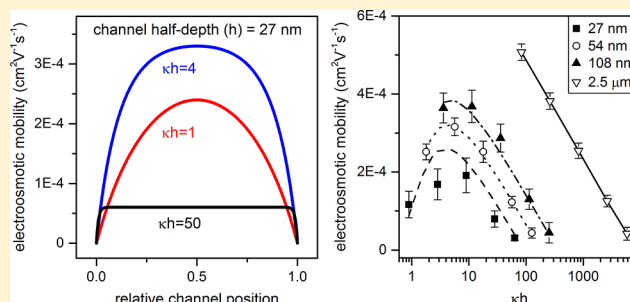
N anofluidic devices have received considerable attention due to their unique ion and fluid transport properties[1,2] and applications in chemical analysis.[3,4] Small lateral dimensions, surface charge, and geometric asymmetry contribute to many of these interesting transport phenomena. Nanochannel devices exhibit concentration polarization and are able to concentrate small molecules[5] and peptides and proteins[6,7] at the nanochannel and microchannel interface. Electrokinetically mediated transport through nanoporous membranes[8] can be used to create chemical gradients,[9] concentrate mass-limited samples,[10] and stack samples[11] across microfluidic layers separated by a membrane. When the nanoscale conduit has a geometric asymmetry, ion current rectification occurs in quartz nanopipettes,[12,13] track-etched polymer membranes,[14−16] silicon-based nanochannels,[17] and nanoscale funnels.[18] Conical nanopores can electrokinetically trap and concentrate particles due to the high electric field strength at the tips of the pores.[19,20] Within nanochannel devices, enhanced channel conductance[21] and reduced electrokinetic mobilities of small molecules[22] and DNA[23] are observed. Nanochannel devices are also used for resistive-pulse sensing of single molecules,[24] ion current rectification-based sensing,[17] and separations based on entropic sieving,[25] liquid chromatography,[26] electrophoresis,[22] and continuous-flow Ogston and entropic sieving.[27]

Nanofluidic devices with in-plane nanochannels have been fabricated in a variety of materials by techniques such as wet chemical etching,[25,27,28] double thermal oxidation and wet chemical etching,[29] sacrificial layer deposition,[30] nanoimprint lithography,[31] focused ion beam (FIB) milling,[32] electron-beam (e-beam) lithography with reactive-ion etching,[33] and e-beam lithography and polymer replication.[18,34] Fabrication techniques, such as e-beam lithography and FIB milling, are able to create channels confined to nanometer dimensions in both lateral dimensions, e.g., width and depth, and to generate any two-dimensional channel pattern on the substrate surface. FIB milling has the added advantage to directly mill channels with three-dimensional topography during a single fabrication step. We milled the nanofluidic channels directly into borosilicate glass with an FIB instrument, which uses an electron flood gun to minimize surface charge generated by the ion beam. Use of the electron flood gun circumvented the need for a conductive film, e.g., metal, on the glass surface to dissipate charge buildup.

In particular, we are interested in electroosmotic flow in nanochannels when κh is small, where κ is the Debye−Hückel parameter[35] and h is the channel half-depth. Electroosmotic mobility decreases as the channel dimension (e.g., h) becomes small, the Debye length (κ^{-1}) becomes large, or both.[36,37] As the double layer extends into the channel, the profile for electroosmotic flow goes from having a uniform velocity profile to a nonuniform profile with a reduced average velocity. As κh approaches 1, double layer overlap occurs, the flow profile becomes parabolic, and electroosmotic mobility reaches a minimum for a given Debye length. This theory was extended to include an analytical solution for a cylindrical capillary[38] and parallel-plate channel.[39]

Subsequent work about electroosmotic flow in nanochannels is mostly theoretical.[40,41] Numerical simulations of electrokinetically driven fluids address the influence of channel dimensions,[42,43] double layer thickness and electrostatic potential distribution,[44,45] surface potential,[46] and ion valence[47] on electroosmotic flow. Similar to early work,[36−39] finite element analysis predicts the reduction of electroosmotic velocities when there is double layer overlap in the channel.[48] Simulations also study the validity of common approximations, in particular, the linear solution of the Poisson−Boltzmann equation to calculate potential distributions when the surface potential is relatively high or the electrostatic potential in the center of the channel is zero.[49] Two-dimensional flow profiles are generated for cases in which there is significant double layer overlap in nanochannels to account for sidewall effects.[50−52] Reduction of electroosmotic velocity due to the double layer extending into the nanochannel is observed experimentally at low buffer concentrations in high aspect ratio channels.[22,53] Also, electroosmotic flow is measured in nanochannels with no double layer overlap by a current-monitoring technique.[54,55]

We measured the average electroosmotic mobilities and ionic conductivities in channels with half-depths of 27 nm, 54 nm, 108 nm, and 2.5 μm for NaCl concentrations from 0.1 to 500 mM. From these micro- and nanochannels measurements, specific surface charge, zeta (ζ) potentials, and electroosmotic mobilities are extracted directly from the experimental data. The experimental electroosmotic mobilities compare quantitatively to mobilities calculated from a nonlinear solution of the Poisson−Boltzmann equation for channels with a parallel-plate geometry. For the calculations, ζ-potentials measured in the 2.5 μm channel are used and range from −6 to −73 mV for 500 to 0.1 mM NaCl, respectively. For $\kappa h > 50$, electroosmotic mobilities in the nanochannels are accurately predicted by the Smoluchowski equation.[56] However, for $\kappa h < 10$, the electrical double layer extends into the nanochannels, and due to confinement in the channels, average electroosmotic mobilities decrease. At $\kappa h \approx 4$, electroosmotic mobilities in the 27, 54, and 108 nm channels exhibit maxima, and at 0.1 mM NaCl, the electroosmotic mobility in the 27 nm channel ($\kappa h = 1$) is 5-fold lower than the electroosmotic mobility in the 2.5 μm channel ($\kappa h = 100$).

■ EXPERIMENTAL SECTION

Materials. We purchased chromium etchants 1020 and 8002-A and buffered oxide etchant (BOE) from Transene Co.; Microposit MF 319 developer from MicroChem Corp.; D263 glass substrates with a 530 nm thick layer of photoresist and a 120 nm thick layer of chromium from Telic Co.; No. 1.5 cover glass from VWR; rhodamine B and disodium fluorescein from Sigma-Aldrich Co.; NaCl and NaOH from Mallinckrodt, Inc.; methanol from EMD Millipore, Inc.; and 353NDT Epoxy from Epoxy Technology, Inc.

Microchannel Fabrication. We fabricated microfluidic devices with and without integrated nanochannels. For the devices with nanochannels, two V-shaped microchannels were fabricated in a glass substrate by conventional photolithography and wet chemical etching, and the nanochannel was milled into the substrate to bridge the gap between the two microchannels (Figure 1). The V-shaped microchannel design was transferred into the photoresist layer by UV exposure (200 mJ/cm^2) through a photomask (HTA Photomask). After development of the photoresist, the chromium layer was etched with chromium etchant 8002-A, and the microchannels were etched into the
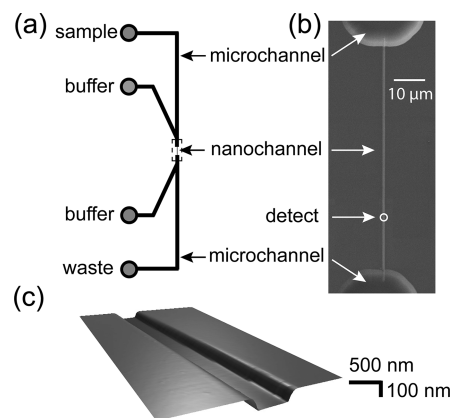

Figure 1. (a) Schematic of a nanochannel device used for electroosmotic mobility and conductivity measurements. Two V-shaped microchannels (represented by thick black lines) are bridged by a nanochannel milled with a focused ion beam (FIB) instrument. (b) Scanning electron microscope (SEM) image of an FIB-milled nanochannel with a half-depth of 54 nm, half-width of 265 nm, and length of 76 μm that bridges two microchannels etched into the glass substrate. Arrival of rhodamine B dye is detected 60 μm from the top micro- and nanochannel junction at the "detect" location. (c) Atomic force microscope (AFM) image of a nanochannel with a half-depth of 54 nm and half-width of 265 nm.

glass substrate with BOE. The microchannels were measured with a stylus-based profiler (Dektak 6M, Veeco Instruments, Inc.) and had a half-depth of 2.55 ± 0.2 μm and a width of 31 ± 2 μm. Holes were sandblasted into the backside of the substrate for fluid and electrical access at the ends of the microchannels. Remaining photoresist and chromium were then removed with acetone and chromium etchant 1020, respectively, and the glass surfaces were cleaned in an ammonium hydroxide, hydrogen peroxide, and water solution (2:1:2), rinsed with water, and dried before FIB milling as described below. For microfluidic devices without nanochannels, microchannels with a cross pattern were fabricated by the same process as above. The cross-shaped microchannels had a half-depth of 2.52 ± 0.2 μm and a width of 42 ± 2 μm.

Nanochannel Fabrication. Nanochannels were milled between the two V-shaped microchannels with a dual-beam FIB instrument (AURIGA 60, Carl Zeiss, Inc.). Nanochannels with a rectangular design were created in the NanoPatterning and Visualization Engine (FIBICS Corp.), and a 30 kV gallium ion beam at 50 pA milled the pattern directly into the glass while an electron flood gun bathed the substrate surface with electrons to compensate for charge buildup. After FIB milling, the nanochannels were characterized with the scanning electron microscope (SEM) on the FIB instrument and an atomic force microscope (AFM; MFP-3D, Asylum Research) to determine the nanochannel dimensions. All of the nanochannels had a length of 76 ± 2 μm (i.e., the distance between the two V-shaped microchannels) and half-widths of 265 ± 10 nm. We fabricated three nanochannel devices with half-depths of 27 ± 2 nm, four nanochannel devices with half-depths of 54 ± 3 nm, and two nanochannel devices with half-depths of 108 ± 5 nm.

Device Bonding. Substrates with and without integrated nanochannels and No. 1.5 cover glass were soaked in 1 M NaOH at 60 °C for 20 min, sonicated in water for 10 min, rinsed with water, and brought into contact with each other while wet. The bonded devices were dried in an oven at 90 °C overnight and annealed in a furnace at 545 °C for 12 h. Glass

reservoirs (6 mm o.d. × 4 mm i.d. × 6 mm tall) were attached over the sandblasted holes with epoxy to hold the solutions and make electrical connections to the micro- and nanochannels.

Nanochannel Conditioning. After bonding, micro- and nanochannels in the devices were sequentially rinsed with methanol, 1:1 methanol in water, water, 1 M NaOH, and water. Solutions were drawn through the channels with vacuum for 15 min each. Devices filled with water were stored for at least 4 days before measurements were made to ensure reproducible electroosmotic flow. Electroosmotic flow increased slightly from days 1 to 3, but by day 4, no significant change in electroosmotic mobility was observed. The change in mobility is presumably due to the dissolution of Ga ions at the glass surface that were deposited during the FIB milling process.

Conductivity Measurements. Channel conductivities for each device were measured with a picoammeter/voltage source (6487 Keithley Instruments, Inc.). Silver–silver chloride electrodes were prepared by sanding a 10 mm section of a 2 mm diameter piece of silver wire and immersing this section of wire in an $FeCl_3$ chloridizing solution overnight.[57] The chloridized sections of the electrodes were placed in the solution-filled reservoirs, and the nonchloridized sections were wired to the voltage source. With 1 V applied through silver–silver chloride electrodes, the current was measured between each pair of reservoirs on a device, and channel conductance was calculated from the average current for each micro- and nanochannel by a least-squares method. Channel conductivities were then calculated with the channel length and cross-sectional area. We tested NaCl solutions of 0.1, 1, 10, 100, 500, and 1000 mM (pH 5.1−5.5). Channel conductivities were measured on three 27 nm channels, four 54 nm channels, two 108 nm channels, and two 2.5 μm channels. The bulk conductivity of each solution was measured with a standard conductivity meter (1026, VWR, Inc.).

Electroosmotic Flow Measurements. In the nanochannel devices, we measured the electroosmotic velocity by monitoring the arrival time of a zwitterionic dye (rhodamine B) at a location 60 μm from the micro- and nanochannel junction (the location labeled "detect" in Figure 1b). The arrival time of the rhodamine B was monitored on an inverted optical microscope (IX71, Olympus, Inc.), and a green helium−neon laser focused to a spot with a 60× objective at the detection location was used to excite the dye. The fluorescence was collected by the objective, spectrally filtered with the bandpass filter in the TRITC filter cube (U-N41002, Olympus, Inc.), spatially filtered with a 100 μm pinhole, detected with a photomultiplier tube (H5783-01, Hamamatsu Photonics), amplified (SR570, Stanford Research Systems, Inc.), and recorded through a multifunction data acquisition card (PCI-6032, National Instruments Corp.) with a LabVIEW program (National Instruments Corp.).

A positive potential (0.3−5.2 V) from an analog output card (PCI-6713, National Instruments Corp.) controlled through the LabVIEW program was applied through a silver–silver chloride electrode to the sample reservoir (see Figure 1a), and a silver–silver chloride electrode inserted into the waste reservoir was held at ground. For each set of measurements, the NaCl concentration was stepped from lowest (0.1 mM) to highest (500 mM), and the field strength was stepped from lowest (50 V/cm) to highest (250 V/cm). The arrival time distribution of the dye front in nanochannels was fitted with a sigmoidal curve, and the arrival time corresponded to the half-height of the curve. Arrival times of the rhodamine B solution at the

detection point ranged from 70 ms to 1.40 s for the low-salt concentrations at high field strengths and the high-salt concentrations at low field strengths, respectively. The time for rhodamine B to diffuse 60 μm is estimated to be ∼4 s and did not impact the electroosmotic flow measurements.

To measure the electroosmotic mobility on the cross-shaped microchannel device, we used a pinched injection[58] and monitored the arrival time of rhodamine B 4 mm downstream from the cross intersection. Potentials were applied to the reservoirs with a high-voltage power supply controlled by a LabVIEW program. For measurements made in both the nanochannel and microchannel devices, the electroosmotic mobility was calculated from a linear fit of electroosmotic velocity versus field strength. Similar to the conductivity measurements, electroosmotic mobilities were measured in three 27 nm channels, four 54 nm channels, two 108 nm channels, and two 2.5 μm channels. To check for concentration polarization, disodium fluorescein (10 μM) was added to the NaCl solutions and drawn into devices with the 27 nm channel for 15 min by vacuum. Potentials of 1 and 10 V, corresponding to field strengths of 120 and 1200 V/cm in the nanochannels, respectively, were applied, and the microchannel and nanochannel junctions were visualized on the inverted IX71 microscope by wide-field epifluorescence.

■ RESULTS AND DISCUSSION

Nanochannel Fabrication. Rectangular nanochannels were fabricated in the gap between two closely spaced V-shaped microchannels (see Figure 1). The microchannels were fabricated by standard photolithography and wet chemical etching, and the nanochannels were milled into the glass substrate between the microchannels with a focused ion beam. We used an electron flood gun to minimize charge buildup at the substrate surface caused by the ion beam. Each of the milled nanochannels had a length of 76 ± 2 μm and width ($2w$) of 530 ± 10 nm, but had depths ($2h$) of 54 ± 4, 108 ± 6, or 216 ± 10 nm. We used an SEM to measure the nanochannel width and an AFM to determine the nanochannel depth. To facilitate comparison to theory, we refer to the channels by their half-depths (h) of 27, 54, and 108 nm. SEM and AFM images of a nanochannel with a 54 nm half-depth are shown in Figure 1b,c.

Channel Conductivity. We measured the ionic conductivities in the nanochannels with half-depths of 27, 54, and 108 nm for NaCl solutions from 0.1 to 1000 mM and compared their conductivities with the conductivities of the bulk solutions and a microchannel with a half-depth of 2.5 μm. At a fixed potential of 1 V, currents in the micro- and nanochannels were measured, and channel conductance is calculated from these current measurements recorded for each reservoir pair. Channel conductivities are then calculated from the channel conductance and measured channel lengths and cross-sectional areas of the micro- and nanochannels.

Figure 2 shows the variation of the channel conductivity with NaCl concentration and bulk solution conductivity. As expected, at high salt concentrations, the nanochannel conductivities match the bulk solution conductivities. However, at low salt concentrations, the nanochannel conductivities deviate from linearity and are significantly higher than the conductivities in the microchannel and bulk solution.[18,21,59] The deviation increases as the channel half-depth decreases, i.e., the shallowest nanochannel (h = 27 nm) has the highest conductivities for NaCl concentrations of 0.1, 1, and 10 mM. Deviation from linearity occurs because a significant portion of
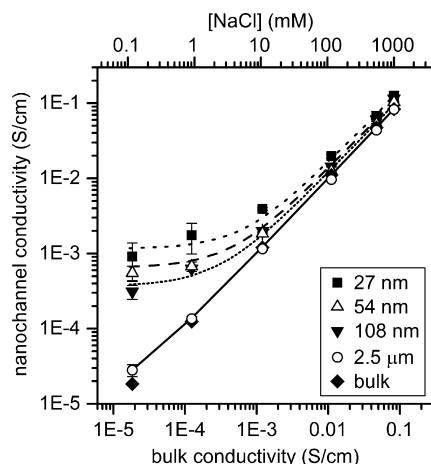
Figure 2. Variation of channel conductivity with bulk conductivity and NaCl concentration. Channel half-depths (h) are 27 nm, 54 nm, 108 nm, and 2.5 μm. Lines for each channel half-depth are calculated with eq 1 from the specific surface conductivities, bulk conductivities, and channel dimensions. Measurements were made on three devices with h = 27 nm, four devices with h = 54 nm, and two devices with h = 108 nm and 2.5 μm. Error bars are $\pm$ σ.

Figure 3. Variation of specific surface conductivity (λ_s) and zeta potential (ζ-potential) with bulk conductivity and NaCl concentration. The specific surface conductivities are an average for all nanochannel and microchannel devices and were measured on three devices with h = 27 nm, four devices with h = 54 nm, and two devices with h = 108 nm and 2.5 μm. ζ-potentials were measured on two devices with h = 2.5 μm. Error bars are $\pm$ σ.

the current is carried through the nanochannel by surface charge. As the surface-to-volume ratio of the channel increases, surface charge contributes a much greater fraction of current transported, which results in higher channel conductivities.

The experimental channel conductivities are in excellent agreement with the model presented by Hunter[56] adapted to a channel with a rectangular cross-section. Equation 1 shows the channel conductivity, σ_c:

$$\sigma_c = \sigma_b + \lambda_s\left(\frac{1}{h} + \frac{1}{w}\right) \tag{1}$$

where σ_b is the bulk solution conductivity, λ_s is the specific surface conductivity, and w is the channel half-width. λ_s is calculated from eq 1 with an average of three conductivity measurements from each channel dimension at each salt concentration. Figure 3 shows the average λ_s for all channel depths, which ranged from 2.15 to 137 nS for NaCl concentrations of 0.1 to 1000 mM, respectively. When the channel cross-section is large, i.e., h and w are large, the second term of eq 1 for the contribution of the surface charge goes to zero, and the channel conductivity matches the bulk conductivity. However, when h and w are small, the second term becomes significant, and the channel conductivity is greater than the bulk conductivity. Equation 1 is used to calculate the channel conductivities from the specific surface conductivities, bulk conductivities, and channel dimensions for each channel half-depth, and the predicted values (lines in Figure 2) match the experimental data for all channel dimensions across all concentrations.

Electroosmotic Mobility. The electroosmotic velocity was measured in the channels with h = 27 nm, 54 nm, 108 nm, and 2.5 μm. The zwitterionic dye, rhodamine B, was added to NaCl solutions of 0.1 to 500 mM and detected by laser-induced fluorescence. For the nanochannel devices, a front of the rhodamine B solution was introduced into the nanochannel, and the arrival time of the dye was detected 60 μm from the top micro- and nanochannel junction (the location labeled "detect" in Figure 1b). For the microchannel devices, a pinched injection[58] was used to introduce a plug of rhodamine B
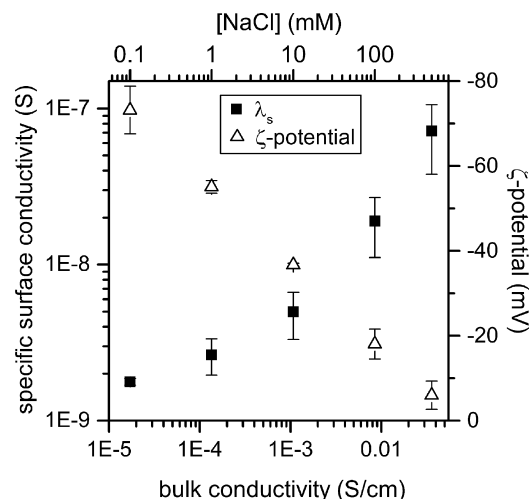
solution, and the arrival time of the rhodamine B plug was detected 4 mm downstream from the cross intersection. Over the range of electric field strengths used (50−250 V/cm), the electroosmotic velocity was linear with field strength for all NaCl concentrations. The slopes of the lines fitted to the velocity versus field strength data are the electroosmotic mobilities in the micro- and nanochannels. For the linear fits, R^2 > 0.999 for the experiments with the 0.1−100 mM NaCl solutions, and R^2 > 0.998 for the experiments with the 500 mM NaCl solution.

To evaluate whether concentration polarization might impact the conductivity and electroosmotic flow measurements, we imaged the transport of fluorescein through the nanochannels with applied potentials of 1 and 10 V, and enrichment or depletion of the fluorescein at the entrance or exit of the nanochannel was not observed. Although some concentration polarization may occur, the time scale for each electroosmotic flow measurement was relatively short, e.g., 1−5 s in duration, because the polarity of the power supply was switched frequently to move rhodamine B into the nanochannel and clear the dye from the nanochannel for the next measurement. In addition, the channel conductivities and electroosmotic mobilities in the nanochannels are consistent with values measured in the microchannels, for which concentration polarization is negligible (see Figures 2 and 4).

Figure 4 shows the variation of electroosmotic mobility with Debye length (κ^{-1}). For NaCl concentrations of 0.1 to 500 mM, the Debye lengths for a 1:1 electrolyte at 22 °C range from 30 to 0.4 nm, respectively.[35] As expected, the electroosmotic mobilities in the 2.5 μm channel are linear over the entire NaCl concentration range. However, the electroosmotic mobilities in the three nanochannels at low salt concentrations (0.1, 1, and 10 mM) are significantly reduced compared to the electroosmotic mobilities in the microchannel. Reduction of the electroosmotic mobility is most pronounced in the 27 nm channel with κ^{-1} = 30 nm for 0.1 mM NaCl, where double layer overlap results in a parabolic flow profile with a reduced average mobility compared to the flat-flow profile in microchannels
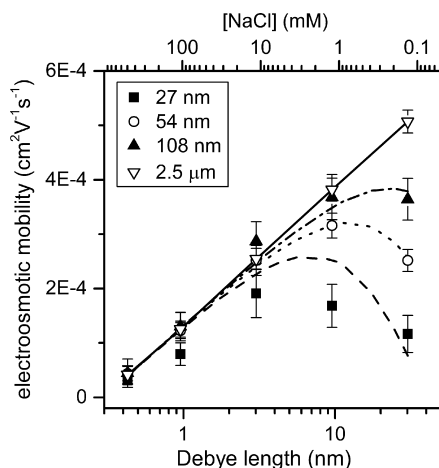
Figure 4. Variation of average electroosmotic mobility (μ_{eo}) with Debye length (κ^{-1}) for channel half-depths (h) of 27 nm, 54 nm, 108 nm, and 2.5 μm and NaCl concentrations from 0.1 to 500 mM. Lines for each channel half-depth are calculated with eq 4. Measurements were made on three devices with h = 27 nm, four devices with h = 54 nm, and two devices with h = 108 nm and 2.5 μm. Error bars are $\pm \sigma$.

Figure 5. Variation of average electroosmotic mobility (μ_{eo}) with κh for channel half-depths (h) of 27 nm, 54 nm, 108 nm, and 2.5 μm and NaCl concentrations from 0.1 to 500 mM. Lines for each channel half-depth are calculated with eq 4. Measurements were made on three devices with h = 27 nm, four devices with h = 54 nm, and two devices with h = 108 nm and 2.5 μm. Error bars are $\pm \sigma$.

with a higher average mobility.[36,37,39] In addition, the electroosmotic mobilities in the nanochannels milled by the FIB instrument are in excellent agreement with the electroosmotic mobilities in the microchannels etched by a wet-chemical method. The electroosmotic mobilities in the 2.5 μm channel coincide with the electroosmotic mobilities in the 108 nm channel for NaCl concentrations $\geq$1 mM, in the 54 nm channel for NaCl concentrations $\geq$10 mM, and in the 27 nm channel for NaCl concentrations $\geq$100 mM. These results suggest that the FIB-milling process does not significantly impact the surface and ζ-potential of the nanochannels.

Theoretical electroosmotic mobilities are calculated from a nonlinear solution of the Poisson−Boltzmann equation for a channel with parallel-plate geometry.[43] The equilibrium potential, $\psi(y)$, in the channel at position y perpendicular to the wall is calculated:

$$\psi(y) = \frac{4kT}{ze}\left[\tanh^{-1}\left(\tanh\left[\frac{ze\zeta}{4kT}\right]\exp(-\kappa y)\right)\right] + \frac{4kT}{ze}\left[\tanh^{-1}\left(\tanh\left[\frac{ze\zeta}{4kT}\right]\exp(-\kappa(2h-y))\right)\right] \quad (2)$$

where k is the Boltzmann constant, T is the temperature, z is the ion valence, and e is the electronic charge. The electroosmotic velocity, $u_{eo}(y)$, is calculated:

$$u_{eo}(y) = -\frac{\varepsilon\zeta E}{\eta}\left(1 - \frac{\psi(y)}{\zeta}\right) \quad (3)$$

where ε is the permittivity of the medium, η is the viscosity, and E is the electric field strength. ζ-potentials measured in the 2.5 μm channel ranged from −6 to −73 mV for NaCl concentrations from 500 to 0.1 mM, respectively (see Figure 3) and are used in these calculations.

The average electroosmotic mobility, μ_{eo}, is then calculated by eq 4:

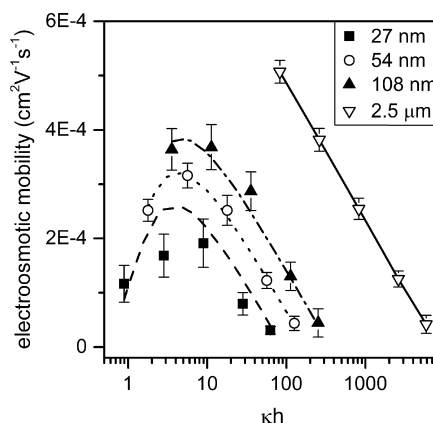$$\mu_{eo} = \frac{1}{2hE}\int_0^{2h} u_{eo}(y)\,dy \quad (4)$$

μ_{eo} is integrated from the channel wall ($y = 0$) across the entire channel depth ($y = 2h$). The permittivity of the medium and solution viscosity for water are used and assumed to be constant. Calculated values of μ_{eo} for each nanochannel half-depth are plotted as lines in Figures 4 and 5 and match the experimental data extremely well over the entire range of NaCl concentrations.

For large κh where κ is the Debye−Hückel parameter, the ratio $\psi(y)/\zeta$ goes to zero, and eq 3 for u_{eo} reduces to the Smoluchowski equation.[56] For small κh, $\psi(y)/\zeta$ approaches 1, and u_{eo} is significantly reduced in the channel. Figure 5 shows the variation of electroosmotic mobility with κh. In the microchannel, $\kappa h > 100$ for all electroosmotic mobility measurements, and therefore, the electroosmotic mobilities are linear with κh. For $\kappa h > 50$, electroosmotic mobilities in the nanochannels are accurately predicted by the Smoluchowski equation. However, for $\kappa h < 10$, the electrical double layer extends into the nanochannel, and consequently, electroosmotic mobilities decrease as the nanochannel half-depths decrease. In Figure 5, maxima in the electroosmotic mobilities are observed at $\kappa h \approx 4$ for all three nanochannels, and the experimental data are in excellent agreement with predicted values. These maxima occur at different NaCl concentrations for all three nanochannels (see Figure 4) and indicate that the degree of double layer overlap depends on both channel dimensions and Debye length. Moreover, at $\kappa h \approx 4$ where the average electroosmotic mobilities exhibit maxima, the electrostatic potential in the center of the channel is zero. When κh goes from 4 toward 1, the electrostatic potential in the channel center becomes nonzero due to interaction between the electrical double layers, and consequently, the average electroosmotic mobilities decrease.

Equation 2 is a nonlinear solution of the Poisson−Boltzmann equation that assumes a two-dimensional flow field in channels with a parallel-plate geometry and neglects sidewall effects.[43] Our nanochannels are shallow rectangles and have aspect ratios (w/h) of 9.8, 4.9, and 2.5 for channel half-depths of 27, 54, and 108 nm, respectively. The calculated electroosmotic mobilities match the experimental values for the 54 and 108 nm channels, which have the lower aspect ratios. The 27 nm channel has the highest aspect ratio of the channels tested, and except for one

point at $\kappa h = 2.8$, the calculated and experimental electroosmotic mobilities match. In our calculation, we use the ζ-potentials measured in the 2.5 μm channel and do not account for possible changes in the surface charge density as κh approaches 1.[60] Consequently, suppression of the electroosmotic flow is simply due to geometric confinement of the electrical double layer in the shallow nanochannels. The model also assumes weak double layer overlap ($\kappa h \geq 2$).[43] This assumption is considered valid for all of our electroosmotic flow measurements except two measurements made at 0.1 mM NaCl in the 27 nm channel ($\kappa h = 1$) and 54 nm channel ($\kappa h = 1.8$). However, as seen in Figures 4 and 5, the calculated and experimental values match well.

CONCLUSION

Nanochannels with rectangular cross sections fabricated in glass by FIB milling show enhanced ionic conductivities and reduced electroosmotic mobilities when compared to ion and electroosmotic transport in microchannels. These nanochannels have large surface-to-volume ratios, and consequently, the surface conductivity dominates the ionic conductivity in the channel. Also, as the Debye length becomes comparable to the channel half-depth (e.g., $\kappa h < 10$), the electrical double layer extends into the channel and significantly impacts the electroosmotic flow profile, which leads to a lower average electroosmotic velocity. The experimental electroosmotic mobilities match theoretical predictions, and both exhibit maxima at $\kappa h \approx 4$.

AUTHOR INFORMATION

Corresponding Author
*Phone: +1-812-855-6620 . E-mail: jacobson@indiana.edu.

Notes
The authors declare no competing financial interest.

ACKNOWLEDGMENTS

REFERENCES

(1) Schoch, R. B.; Han, J.; Renaud, P. *Rev. Mod. Phys.* **2008**, *80*, 839−883.
(2) Zangle, T. A.; Mani, A.; Santiago, J. G. *Chem. Soc. Rev.* **2010**, *39*, 1014−1035.
(3) Kovarik, M. L.; Jacobson, S. C. *Anal. Chem.* **2009**, *81*, 7133−7140.
(4) Piruska, A.; Gong, M.; Sweedler, J. V.; Bohn, P. W. *Chem. Soc. Rev.* **2010**, *39*, 1060−1072.
(5) Pu, Q.; Yun, J.; Temkin, H.; Liu, S. *Nano Lett.* **2004**, *4*, 1099−1103.
(6) Wang, Y.-C.; Stevens, A. L.; Han, J. *Anal. Chem.* **2005**, *77*, 4293−4299.
(7) Kim, S. J.; Wang, Y. C.; Lee, J. H.; Jang, H.; Han, J. *Phys. Rev. Lett.* **2007**, *99*, 044501.
(8) Kemery, P. J.; Steehler, J. K.; Bohn, P. W. *Langmuir* **1998**, *14*, 2884−2889.
(9) Fa, K.; Tulock, J. J.; Sweedler, J. V.; Bohn, P. W. *J. Am. Chem. Soc.* **2005**, *127*, 13928−13933.
(10) Kim, B. Y.; Swearingen, C. B.; Ho, J. A. A.; Romanova, E. V.; Bohn, P. W.; Sweedler, J. V. *J. Am. Chem. Soc.* **2007**, *129*, 7620−7626.
(11) Zhou, K.; Kovarik, M. L.; Jacobson, S. C. *J. Am. Chem. Soc.* **2008**, *130*, 8614−8616.
(12) Wei, C.; Bard, A. J.; Feldberg, S. W. *Anal. Chem.* **1997**, *69*, 4627−4633.
(13) Umehara, S.; Pourmand, N.; Webb, C. D.; Davis, R. W.; Yasuda, K.; Karhanek, M. *Nano Lett.* **2006**, *6*, 2486−2492.
(14) Siwy, Z.; Fulinski, A. *Phys. Rev. Lett.* **2002**, *89*, 198103.
(15) Siwy, Z. S. *Adv. Funct. Mater.* **2006**, *16*, 735−746.
(16) Kovarik, M. L.; Zhou, K.; Jacobson, S. C. *J. Phys. Chem. B* **2009**, *113*, 15960−15966.
(17) Karnik, R.; Duan, C.; Castelino, K.; Daiguji, H.; Majumdar, A. *Nano Lett.* **2007**, *7*, 547−551.
(18) Perry, J. M.; Zhou, K.; Harms, Z. D.; Jacobson, S. C. *ACS Nano* **2010**, *4*, 3897−3902.
(19) Lee, S.; Zhang, Y. H.; White, H. S.; Harrell, C. C.; Martin, C. R. *Anal. Chem.* **2004**, *76*, 6108−6115.
(20) Kovarik, M. L.; Jacobson, S. C. *Anal. Chem.* **2008**, *80*, 657−664.
(21) Stein, D.; Kruithof, M.; Dekker, C. *Phys. Rev. Lett.* **2004**, *93*, 035901.
(22) Pennathur, S.; Santiago, J. G. *Anal. Chem.* **2005**, *77*, 6782−6789.
(23) Menard, L. D.; Ramsey, J. M. *Anal. Chem.* **2013**, *85*, 1146−1153.
(24) Saleh, O. A.; Sohn, L. L. *Nano Lett.* **2003**, *3*, 37−38.
(25) Han, J.; Craighead, H. G. *Science* **2000**, *288*, 1026−1029.
(26) Ishibashi, R.; Mawatari, K.; Kitamori, T. *Small* **2012**, *8*, 1237−1242.
(27) Fu, J.; Schoch, R. B.; Stevens, A. L.; Tannenbaum, S. R.; Han, J. *Nat. Nanotechnol.* **2007**, *2*, 121−128.
(28) Mao, P.; Han, J. Y. *Lab Chip* **2005**, *5*, 837−844.
(29) Persson, F.; Thamdrup, L. H.; Mikkelsen, M. B. L.; Jaarlgard, S. E.; Skafte-Pedersen, P.; Bruus, H.; Kristensen, A. *Nanotechnology* **2007**, *18*, 245301.
(30) Karnik, R.; Castelino, K.; Fan, R.; Yang, P.; Majumdar, A. *Nano Lett.* **2005**, *5*, 1638−1642.
(31) Guo, L. J.; Cheng, X.; Chou, C.-F. *Nano Lett.* **2004**, *4*, 69−73.
(32) Menard, L. D.; Ramsey, J. M. *Nano Lett.* **2011**, *11*, 512−517.
(33) Harms, Z. D.; Mogensen, K. B.; Nunes, P. S.; Zhou, K.; Hildenbrand, B. W.; Mitra, I.; Tan, Z.; Zlotnick, A.; Kutter, J. P.; Jacobson, S. C. *Anal. Chem.* **2011**, *83*, 9573−9578.
(34) Kovarik, M. L.; Jacobson, S. C. *Anal. Chem.* **2007**, *79*, 1655−1660.
(35) Bard, A. J.; Faulkner, L. R. *Electrochemical Methods*; John Wiley and Sons: New York, 1980.
(36) Burgreen, D.; Nakache, F. R. *J. Phys. Chem.* **1964**, *68*, 1084−1091.
(37) Rice, C. L.; Whitehead, R. *J. Phys. Chem.* **1965**, *69*, 417−424.
(38) Levine, S.; Marriott, J. R.; Neale, G.; Epstein, N. *J. Colloid Interface Sci.* **1975**, *52*, 136−149.
(39) Levine, S.; Marriott, J. R.; Robinson, K. *J. Chem. Soc., Faraday Trans. 2* **1975**, *71*, 1−11.
(40) Sparreboom, W.; van den Berg, A.; Eijkel, J. C. T. *New J. Phys.* **2010**, *12*, 015004.
(41) Abgrall, P.; Nguyen, N. T. *Anal. Chem.* **2008**, *80*, 2326−2341.
(42) Conlisk, A. T.; McFerran, J.; Zheng, Z.; Hansford, D. *Anal. Chem.* **2002**, *74*, 2139−2150.
(43) Garcia, A. L.; Ista, L. K.; Petsev, D. N.; O'Brien, M. J.; Bisong, P.; Mammoli, A. A.; Brueck, S. R. J.; Lopez, G. P. *Lab Chip* **2005**, *5*, 1271−1276.
(44) Bhattacharyya, S.; Zheng, Z.; Conlisk, A. T. *J. Fluid Mech.* **2005**, *540*, 247−267.
(45) Pennathur, S.; Santiago, J. G. *Anal. Chem.* **2005**, *77*, 6772−6781.
(46) Qiao, R.; Aluru, N. R. *Langmuir* **2005**, *21*, 8972−8977.
(47) Zheng, Z.; Hansford, D. J.; Conlisk, A. T. *Electrophoresis* **2003**, *24*, 3006−3017.
(48) Yuan, Z.; Garcia, A. L.; Lopez, G. P.; Petsev, D. N. *Electrophoresis* **2007**, *28*, 595−610.
(49) Conlisk, A. T. *Electrophoresis* **2005**, *26*, 1896−1912.
(50) Dutta, P.; Beskok, A. *Anal. Chem.* **2001**, *73*, 1979−1986.
(51) Nosrati, R.; Hadigol, M.; Raisee, M.; Nourbakhsh, A. *J. Comput. Theor. Nanosci.* **2012**, *9*, 2228−2239.
(52) Hlushkou, D.; Perry, J. M.; Jacobson, S. C.; Tallarek, U. *Anal. Chem.* **2012**, *84*, 267−274.

(53) Jacobson, S. C.; Alarie, J. P.; Ramsey, J. M. In *Proceedings of the Micro Total Analysis Systems Symposium*; Ramsey, J. M., van den Berg, A., Eds.; Kluwer Academic Publishers: Dordrecht, The Netherlands, 2001; pp 57−59.

(54) Mela, P.; Tas, N. R.; Berenschot, E. J. W.; van Nieuwkasteele, J.; van den Berg, A. *Electrophoresis* **2004**, *25*, 3687−3693.

(55) Mahabadi, K. A.; Rodriguez, I.; Haur, S. C.; van Kan, J. A.; Bettiol, A. A.; Watt, F. *J. Micromech. Microeng.* **2006**, *16*, 1170−1180.

(56) Hunter, R. J. *Zeta Potential in Colloid Science*; Academic Press, Inc.: San Diego, 1981.

(57) Yao, S.; Wang, M. *J. Electrochem. Soc.* **2002**, *149*, H28−H32.

(58) Jacobson, S. C.; Hergenröder, R.; Koutny, L. B.; Warmack, R. J.; Ramsey, J. M. *Anal. Chem.* **1994**, *66*, 1107−1113.

(59) Baldessari, F.; Santiago, J. G. *J. Colloid Interface Sci.* **2009**, *331*, 550−550.

(60) Behrens, S. H.; Grier, D. G. *J. Chem. Phys.* **2001**, *115*, 6716−6721.